

## Optical-model potential in a relativistic quantum field model

M. Jaminon, C. Mahaux, and P. Rochus

*Institut de Physique, Université de Liège, B4000 Liège 1, Belgium*

(Received 25 March 1980; revised manuscript received 11 June 1980)

The average nucleon-nucleus potential at low and medium energy is investigated in the framework of a relativistic quantum field model. Using the same input parameters as Brockmann in his recent study of nuclear ground states, we calculate the self-consistent relativistic Hartree potential at positive energy in the case of infinite nuclear matter and of  $^{16}\text{O}$  and  $^{40}\text{Ca}$ . This potential is the sum of a scalar operator and of the fourth component of a vector operator. We construct its Schrödinger-equivalent potential by eliminating the small component of the Dirac spinor. The central part of this Schrödinger-equivalent potential is in fair agreement with empirical values at low and intermediate energy. Particular attention is paid to the intermediate energy domain, in which the calculated potential is repulsive in the nuclear interior and attractive at the nuclear surface. This is in keeping with some empirical evidence and is similar to results found in the framework of the nonrelativistic Brueckner-Hartree-Fock approximation. The spin-orbit potential of the relativistic Hartree model is also in good agreement with empirical values.

[NUCLEAR REACTIONS Calculated average nuclear field of nuclear matter,  $^{16}\text{O}$  and  $^{40}\text{Ca}$  at positive energy from relativistic Hartree approximation.]

### I. INTRODUCTION

The optical-model potential plays a central role in most analyses of nuclear reaction data. It is thus of great formal and practical interest to investigate to what extent its empirical characteristics can be accounted for by a theory based on the elementary nucleon-nucleon interaction. Most of the available theoretical approaches<sup>1</sup> start from a nonrelativistic nucleon-nucleon interaction which has no connection with the field theory of nuclear forces. Here, we follow another route to the calculation of the optical-model potential. As summarized by Green,<sup>2</sup> it consists in viewing the incoming nucleon as interacting with the meson fields set up by the target nucleons. This approach to the optical potential had been initiated many years ago,<sup>3-7</sup> but recently received renewed interest<sup>8-12</sup> stirred by successes of a relativistic quantum field model of nuclear matter<sup>13-15</sup> and of finite nuclei<sup>16-28</sup> on the one hand, and by the fact that good fits to angular distribution data and to polarization data have been obtained from a phenomenological relativistic optical model<sup>29-33</sup> on the other hand. The present paper is devoted to the study of the real part of the average nucleon-nucleus interaction at positive energy in the framework of the *self-consistent* relativistic Hartree approximation. Until now, the latter had only been applied to nuclear ground states.<sup>16-22</sup> Following these authors of previous works, we include only three meson fields, which correspond to two massive vector mesons ( $\omega$  and  $\phi$ ) and to one massive scalar meson ( $\sigma$ ), respectively.

In Sec. II A, we briefly recall the four-compo-

nent Hartree equation. Then we reduce it to a nonrelativistic Schrödinger form in two different ways: namely, by eliminating the small components (Sec. II B) and by performing a Foldy-Wouthuysen transformation (Sec. II D). Section II C contains a critical discussion of the so-called relativistic correction which is often introduced in empirical analyses of experimental data.<sup>34-36</sup> Section III is devoted to infinite nuclear matter. We first show (Sec. III A) that in this case many of the relations derived in Sec. II take a physically transparent form. In Sec. III B, we make contact with Walecka's<sup>16</sup> relativistic Hartree model for the binding energy of nuclear matter. Sections III C and III D contain some numerical results based on the meson parameters of the one-boson exchange potential of Erkelenz, Holinde, and Machleidt.<sup>37</sup> These meson parameters had previously been used by Brockmann<sup>22</sup> in his study of the ground states of  $^{16}\text{O}$  and  $^{40}\text{Ca}$ . The central and spin-orbit components of the average nucleon-nucleus potential for these two nuclei are studied in Sec. IV E. The comparison with empirical values is satisfactory. It turns out that at intermediate energy the calculated central potential presents a pocket at the nuclear surface.<sup>11</sup> This "wine-bottle bottom" shape is analyzed in Sec. IV D. Section V contains a brief conclusion.

### II. HARTREE APPROXIMATION IN DIRAC AND SCHRÖDINGER FORMS

#### A. The model

As much as possible, we use the same notation as Brockmann<sup>22</sup> and assume that the nucleons only

exchange a massive scalar ( $\sigma$ ) meson and two massive vector ( $\omega$ ,  $\phi$ ) mesons. When treating the meson field operators as classical fields,<sup>4,13</sup> one obtains the following expression for the nuclear Hamiltonian:

$$H = \sum_{\alpha, \alpha'} \int f_{\alpha'}^{\dagger}(\vec{x}) (-i\gamma^0 \vec{\gamma} \cdot \vec{\nabla} + \gamma^0 m) f_{\alpha}(\vec{x}) d^3x b_{\alpha'}^{\dagger} b_{\alpha} \\ + \frac{1}{2} \sum_{\alpha, \alpha', \beta, \beta'} \int f_{\alpha'}^{\dagger}(\vec{x}_1) f_{\beta'}^{\dagger}(\vec{x}_2) \mathcal{V}(|\vec{x}_1 - \vec{x}_2|) f_{\beta}(\vec{x}_2) \\ \times f_{\alpha}(\vec{x}_1) d^3x_1 d^3x_2 b_{\alpha'}^{\dagger} b_{\beta'}^{\dagger} b_{\beta} b_{\alpha}. \quad (2.1)$$

Here,  $[f_{\alpha}(\vec{x})]$  is a complete set of Dirac spinors and  $b_{\alpha}$  ( $b_{\alpha}^{\dagger}$ ) is an annihilation (creation) operator for nucleons in state  $\alpha$ , and

$$\mathcal{V}(|\vec{x}_1 - \vec{x}_2|) \\ = \gamma_0(1)\gamma_0(2) \{ -\mathcal{V}(|\vec{x}_1 - \vec{x}_2|) + \gamma_{\nu}(1)\gamma^{\nu}(2) \\ \times [\mathcal{V}_{\omega}(|\vec{x}_1 - \vec{x}_2|) + \mathcal{V}_{\phi}(|\vec{x}_1 - \vec{x}_2|)] \}, \quad (2.2)$$

with ( $i = \sigma, \omega, \phi$ )

$$\mathcal{V}_i(r) = \frac{g_i^2}{4\pi} \frac{\Lambda_i^2}{\Lambda_i^2 - m_i^2} [r^{-1} \exp(-m_i r) \\ - r^{-1} \exp(-\Lambda_i r)], \quad (2.3)$$

where  $\Lambda_i$  is a cutoff momentum for the meson-nucleon form factor and  $m_i$  is the mass of meson  $i$ . We have omitted retardation effects since they disappear in the Hartree approximation.<sup>22</sup>

We now restrict the discussion to doubly closed-shell nuclei. If one only retains terms which are linear in the coupling constants  $g_i^2$ , and if one omits the Fock terms which arise from antisymmetrization, the self-energy is given by the relativistic Hartree approximation. Then, the wave function  $\Psi^D$  of a single-particle scattering state with total energy

$$E = \epsilon + m \quad (2.4)$$

satisfies the following Dirac equation:

$$[\vec{\alpha} \cdot \vec{p} + \beta m + \beta U_s(r) + U_0(r)] \Psi^D = E \Psi^D. \quad (2.5)$$

Here, the average nucleon-nucleus potential  $\beta U_s + U_0$  is the sum of a scalar

$$\beta U_s(r) = -\beta \int \rho_s(r') \mathcal{V}_{\sigma}(|\vec{r} - \vec{r}'|) d^3r', \quad (2.6)$$

and of the fourth component of a vector

$$U_0(r) = \sum_{i=\omega, \phi} \int \rho(r') \mathcal{V}_i(|\vec{r} - \vec{r}'|) d^3r', \quad (2.7)$$

where  $\rho(r)$  denotes the self-consistent baryon density

$$\rho(r) = \sum_{\alpha=1}^A \Psi_{\alpha}^{D\dagger}(\vec{x}) \Psi_{\alpha}^D(\vec{x}), \quad (2.8)$$

and  $\rho_s(r)$  is the self-consistent scalar density

$$\rho_s(r) = \sum_{\alpha=1}^A \bar{\Psi}_{\alpha}^D(\vec{x}) \Psi_{\alpha}^D(\vec{x}). \quad (2.9)$$

In Eqs. (2.8) and (2.9) the sum runs over the  $A$  lowest bound state solutions of Eq. (2.5). We note that in the Hartree approximation the average potential is real, local, and independent of energy.

### B. Schrödinger form

It is possible to solve directly the Dirac equation (2.5) and to adjust the average potentials  $U_s(r)$  and  $U_0(r)$  to fit the experimental data.<sup>29</sup> However, most analyses of the data are carried out in a nonrelativistic framework. For the purpose of comparing the present relativistic potential with empirical ones, it is thus useful to write the wave equation (2.5) in a Schrödinger-type form. One way of achieving this consists in eliminating the small components  $\Psi_{\zeta}^D$  of  $\Psi^D$  from Eq. (2.5). The resulting equation for the large components  $\Psi_{\zeta}^D$  reads

$$\left( \frac{p^2}{2m} + \tilde{U}_{\sigma}(r; \epsilon) + U_{s0}(r; \epsilon) \frac{\vec{\sigma} \cdot \vec{L}}{r} \right) \Psi_{\zeta}^D = \frac{k_{\infty}^2}{2m} \Psi_{\zeta}^D, \quad (2.10)$$

where  $k_{\infty}$  denotes the relativistic asymptotic momentum

$$k_{\infty}^2 = 2m\epsilon + \epsilon^2, \quad (2.11)$$

while

$$\tilde{U}_{\sigma}(r; \epsilon) = U_{\sigma}(r; \epsilon) - iU_{s0}(r; \epsilon) \vec{\tau} \cdot \vec{p}, \quad (2.12)$$

$$U_{\sigma}(r; \epsilon) = U_s(r) + U_0(r)$$

$$+ (2m)^{-1} [U_s^2(r) - U_0^2(r)] + \frac{\epsilon}{m} U_0(r), \quad (2.13)$$

$$U_{s0}(r; \epsilon) = -[2mD(r)]^{-1} \frac{d}{dr} [D(r)], \quad (2.14)$$

$$D(r) = E + m + U_s(r) - U_0(r). \quad (2.15)$$

If  $G_{\alpha}(r; \epsilon)$  denotes the radial component of  $\Psi_{\zeta}^D$ , the function

$$g_{\alpha}(r; \epsilon) = [D(r)]^{-1/2} G_{\alpha}(r; \epsilon) \quad (2.16)$$

satisfies the Schrödinger-type equation<sup>22</sup>

$$\frac{d^2 g_{\alpha}(r; \epsilon)}{dr^2} + \left\{ k_{\infty}^2 - \frac{l(l+1)}{r^2} - 2m \left[ \tilde{U}_{\sigma}(r; \epsilon) - \frac{1}{r} U_{s0}(r; \epsilon) (\kappa_{\alpha} + 1) \right] \right\} g_{\alpha}(r; \epsilon) = 0, \quad (2.17)$$

where  $\kappa_{\alpha} = \mp(j + \frac{1}{2})$  for  $j = l \pm \frac{1}{2}$ .

Unless otherwise specified, we neglect, henceforth, the very small difference between  $\tilde{U}_g(r; \epsilon)$  and  $U_g(r; \epsilon)$ . We shall accordingly call  $U_g(r; \epsilon)$  the Schrödinger-equivalent potential. Our definition agrees with Noble's.<sup>9</sup> It differs from Brockmann's<sup>22</sup> by the quantity  $\epsilon^2/2m$ , and is more physical since here  $U_g(r; \epsilon) \rightarrow 0$  for  $r \rightarrow \infty$ , unlike Brockmann's definition. We return to this point in Sec. III A.

### C. Comparison with empirical procedure

Let us first show that Eq. (2.17), with the expression (2.11) for  $k_\infty^2$ , is *formally* identical to the Schrödinger equation used in phenomenological analyses of elastic scattering data with relativistic kinematics.

Following Goldberger and Watson,<sup>39</sup> many phenomenologists, see, e.g., Refs. 34–36, assume that the optical-model potential is the fourth component of a Lorentz vector. The corresponding Dirac equation reads

$$(\vec{\alpha} \cdot \vec{p} + \beta m + U_0^{\text{ph}})\Psi = E\Psi, \quad (2.18)$$

where the upper index ph refers to "phenomenological." A partial wave expansion then leads to the radial wave equation [see Eq. (2.17)]

$$\frac{d^2 g_\alpha^{\text{ph}}(r; \epsilon)}{dr^2} + \left\{ k_\infty^2 - \frac{l(l+1)}{r^2} - 2m \left[ U_g^{\text{ph}}(r; \epsilon) - \frac{1}{r} U_{s_0}^{\text{ph}}(r; \epsilon)(\kappa_\alpha + 1) \right] \right\} g_\alpha^{\text{ph}}(r; \epsilon) = 0, \quad (2.19)$$

where, omitting for simplicity derivative terms,

$$U_g^{\text{ph}}(r) = U_0^{\text{ph}}(r) - \frac{1}{2m} [U_0^{\text{ph}}(r)]^2 + U_0^{\text{ph}}(r) \frac{\epsilon}{m}, \quad (2.20a)$$

$$U_{s_0}^{\text{ph}}(r) = -[2m[E + m - U_0^{\text{ph}}(r)]]^{-1} \frac{d}{dr} [E + m - U_0^{\text{ph}}(r)]. \quad (2.20b)$$

In most empirical analyses, the quadratic term  $U_0^{\text{ph}}(r)$  is omitted, and one writes Eq. (2.19) in the form<sup>34-36</sup>

$$\frac{d^2 g_\alpha^{\text{ph}}(r; \epsilon)}{dr^2} + \left\{ k_\infty^2 - \frac{l(l+1)}{r^2} - 2m \left[ \gamma U_0^{\text{ph}}(r) - \frac{1}{r} U_{s_0}^{\text{ph}}(r)(\kappa_\alpha + 1) \right] \right\} g_\alpha^{\text{ph}}(r; \epsilon) = 0, \quad (2.21)$$

where  $\gamma = E/m$  is the "Lorentz factor." Hence, the phenomenological "relativistic" description consists in using Eq. (2.21), where  $U_0^{\text{ph}}(r)$  and  $U_{s_0}^{\text{ph}}(r)$  are taken as independent empirical potentials adjusted in such a way as to fit the experimental data.

By comparing this procedure with our discussion in Sec. II B, we see that this phenomenological prescription does not rest on safe grounds. Indeed, the basic assumption that the original optical-model potential is the fourth component of a vector field is arbitrary. Moreover, the neglect of the quadratic term leaves out interesting features which will be analyzed in Sec. IV D. It would be much better to use the original Dirac equation (2.5) as done by Arnold, Clark, and Mercer.<sup>30</sup> This criticism bears on the interpretation of Eq. (2.21) as a sound relativistic extension of the Schrödinger equation. It does not hinder us from exploiting the formal similarity between Eqs. (2.17) and (2.21), in order to identify the quantity  $U_g(r; \epsilon)$  with the empirical potential  $\gamma U_0^{\text{ph}}(r)$ , and the quantity  $U_{s_0}(r; \epsilon)$  with the empirical potential  $\gamma U_{s_0}^{\text{ph}}(r)$ , and the quantity  $U_{s_0}(r; \epsilon)$  with the empirical spin-orbit potential  $U_{s_0}^{\text{ph}}(r)$ . We note, however,

that this identification is legitimate only if the elastic scattering and polarization cross sections can be obtained in the same way from Eq. (2.17) as from the phenomenological equation (2.21). It can be checked that this is indeed the case on the basis of the equations contained in Refs. 40–42.

### D. Foldy-Wouthuysen transformation

Equation (2.13) shows that the Schrödinger-equivalent potential depends linearly on  $\epsilon$ , with a slope given by  $U_0(r)/m$ . From general field-theoretical arguments, one knows that  $U_0(r)$  is repulsive while  $U_s(r)$  is attractive. Hence, the depth of the Schrödinger-equivalent potential  $U_g(r)$  decreases with increasing  $\epsilon$ ; this is in keeping with empirical evidence. According to the present model, this energy-dependence reflects the growing importance of the repulsive vector potential  $U_0(r)$ . At first sight, this interpretation appears to be at variance with the works of Duerr<sup>4</sup> and of Humphreys.<sup>6</sup> Indeed, these authors ascribed the decrease of  $U_g(r)$  to the decreasing importance of the attractive field  $U_s(r)$  rather than to the increasing importance of the repulsive field  $U_0(r)$ . In the present section, we show that one can re-

cover Duerr's and Humphreys' interpretation provided that the following inequalities hold:

$$\kappa \sim U_0/m \sim U_s/m \sim (v/c)^2 \ll 1. \quad (2.22)$$

The procedure of Foldy and Wouthuysen<sup>43,44</sup> enables one to approximate the Dirac equation by two two-component equations, in the limit (2.22). By performing two successive unitary transformations, one can obtain a Hamiltonian whose odd part is of the order  $\kappa^5$ . Its even part reads

$$\begin{aligned} H^{\text{FW}} = & \beta \left( m + \frac{\vec{p}^2}{2m} - \frac{\vec{p}^4}{8m^3} \right) + \beta U_s + U_0 \\ & - \frac{1}{8m^2} [ \vec{p}^2 (U_0 + \beta U_s) + 2 \vec{p} (U_0 + \beta U_s) \cdot \vec{p} \\ & - 2 \vec{\alpha} \cdot \vec{p} (U_0) \vec{\alpha} \cdot \vec{p} \\ & + 2 \beta \vec{\alpha} \cdot \vec{p} (U_s) \vec{\alpha} \cdot \vec{p} + 4 \beta U_s \vec{p}^2 ], \end{aligned} \quad (2.23)$$

where we dropped terms of order higher than  $\kappa^4$ . This Hamiltonian yields the following wave equation for the large components of the corresponding wave function:

$$\left[ \frac{\vec{p}^2}{2m} + \tilde{U}_e^{\text{FW}}(r; \vec{p}, \epsilon) + \frac{1}{r} U_{\text{so}}^{\text{FW}}(r) \vec{\sigma} \cdot \vec{L} \right] \Psi_{\vec{p}}^{\text{FW}} = \frac{k_{\infty}^2}{2m} \Psi_{\vec{p}}^{\text{FW}}, \quad (2.24)$$

where

$$\tilde{U}_e^{\text{FW}}(r; \vec{p}, \epsilon) = U_e^{\text{FW}}(r; \vec{p}, \epsilon) + U_D(r; \vec{p}), \quad (2.25)$$

with

$$\begin{aligned} U_e^{\text{FW}}(r; \vec{p}, \epsilon) = & U_s(r) + U_0(r) - \frac{1}{2m^2} U_s \vec{p}^2 \\ & - \frac{\vec{p}^4}{8m^3} + \frac{\epsilon^2}{2m}, \end{aligned} \quad (2.26)$$

$$\begin{aligned} U_D(r; \vec{p}) = & \frac{1}{8m^2} [ \nabla^2 (U_0 + U_s) + 2i \vec{\nabla} (U_0 + U_s) \cdot \vec{p} ] \\ & - \frac{i}{r} U_{\text{so}}^{\text{FW}} \vec{p} \cdot \vec{p}, \end{aligned} \quad (2.27)$$

while

$$U_{\text{so}}^{\text{FW}}(r) = -\frac{1}{4m^2} \frac{d}{dr} [ U_s(r) - U_0(r) ]. \quad (2.28)$$

Equation (2.26) establishes our earlier claim that in the limit (2.22) the decrease of the Schrödinger-equivalent potential with increasing energy can be interpreted as a decreasing contribution of  $U_s$  with increasing local momentum. The three first terms on the right-hand side of Eq. (2.26) essentially correspond to the nucleon-nucleus potential considered by Humphreys<sup>6</sup> on the basis of arguments based on the Lorentz contraction of the source of scalar mesons. Although intuitively attractive, Humphreys' reasoning should be con-

sidered as phenomenological. Indeed, this author does not specify in which wave equation his nucleon-nucleus potential should be used. Up to order  $\kappa^2$ , the potential (2.26) had previously been considered by Duerr and by Friar.<sup>45</sup> The difference between  $U_e^{\text{FW}}(r; \vec{p}, \epsilon)$  [Eq. (2.26)] and  $U_e(r; \epsilon)$  [Eq. (2.13)] is at first sight somewhat puzzling. Indeed, the former does not contain a term proportional to  $U_s^2 - U_0^2$  whose importance will appear in Sec. IV D. Furthermore, its momentum dependence is proportional to the scalar field  $U_s(r)$ , while the energy dependence of  $U_e(r; \epsilon)$  is due to the vector field  $U_0(r)$ . The origin of these formal differences will be exhibited in the next section, in the case of infinite nuclear matter.

### III. INFINITE NUCLEAR MATTER

#### A. The single-particle potential

Since the potential felt by a nucleon is a combination of a scalar field ( $\beta U_s$ ) and of the fourth component ( $U_0$ ) of a vector field, the relativistic energy-momentum relation reads

$$(\epsilon + m - U_0)^2 = p^2 + (m + U_s)^2. \quad (3.1)$$

This yields

$$\begin{aligned} \epsilon + \frac{\epsilon^2}{2m} = & \frac{p^2}{2m} + U_s + U_0 + (2m)^{-1} (U_s^2 - U_0^2) \\ & + (m)^{-1} U_0 \epsilon. \end{aligned} \quad (3.2)$$

Equations (2.11) and (2.13) show that this relation is identical to the Schrödinger-type equation (2.10). It can indeed be written in the form

$$\frac{1}{2m} k_{\infty}^2 = \frac{p^2}{2m} + U_e(\epsilon), \quad (3.3)$$

with

$$U_e(\epsilon) = U_s + U_0 + (2m)^{-1} (U_s^2 - U_0^2) + (m)^{-1} U_0 \epsilon. \quad (3.4)$$

Instead of expressing the effective potential  $U_e$  as a function of the energy  $\epsilon$ , let us write it as a function of  $p$ . From Eq. (3.2) one gets the dispersion relation

$$\epsilon = -m + U_0 + [ p^2 + (m^*)^2 ]^{1/2}, \quad (3.5)$$

where the "effective mass"  $m^*$  is defined by<sup>4,13</sup>

$$m^* = m + U_s. \quad (3.6)$$

By inserting expression (3.5) for  $\epsilon$  into Eq. (3.4), one finds

$$U_e(p) = U_s + \frac{1}{2m} (U_s^2 + U_0^2) + \frac{U_0}{m} [ p^2 + (m^*)^2 ]^{1/2}. \quad (3.7)$$

In order to obtain a low-energy approximation, let us expand the right-hand side of Eq. (3.5). In the limit (2.22), and keeping terms up to order  $(v/c)^4$ , one obtains

$$\frac{\epsilon^2}{2m} + \epsilon = \frac{p^2}{2m} + U_s^{\text{FW}}(p; \epsilon), \quad (3.8)$$

where

$$U_s^{\text{FW}}(p; \epsilon) = U_s + U_0 - \frac{1}{2m^2} U_s p^2 - \frac{p^4}{8m^3} + \frac{\epsilon^2}{2m}. \quad (3.9)$$

We recognize in this expression the Foldy-Wouthuysen approximation (2.26) in the case of an infinite medium. One can obtain a better low-energy approximation by expanding the right-hand side of Eq. (3.5) in powers of  $(p/m^*)$ . This yields

$$\epsilon = \frac{p^2}{2m^*} + U_0 + U_s - \frac{p^4}{8(m^*)^3}, \quad (3.10a)$$

which gives

$$\frac{\epsilon^2}{2m} + \epsilon = \frac{p^2}{2m} + U_s^{\text{LE}}(p; \epsilon), \quad (3.10b)$$

where the quantity  $U_s^{\text{LE}}(p; \epsilon)$  is given by

$$U_s^{\text{LE}}(p; \epsilon) = U_s + U_0 - \frac{1}{2m(m+U_s)} p^2 U_s - \frac{1}{8(m+U_s)^3} p^4 + \frac{\epsilon^2}{2m}. \quad (3.11)$$

One can write Eq. (3.8) in the form

$$\epsilon + m = \frac{p^2}{2m} + U_B(\epsilon) + m, \quad (3.12)$$

where

$$U_B(\epsilon) = U_s(\epsilon) - \frac{\epsilon^2}{2m} \quad (3.13)$$

is the quantity introduced by Brockmann.<sup>22</sup> This quantity approaches  $(-\infty)$  as  $\epsilon \rightarrow +\infty$  and should therefore not be identified with the optical-model potential. We pointed out at the end of Sec. II B that in a finite nucleus  $U_B(r; \epsilon)$ , moreover, does not tend towards zero as  $r \rightarrow \infty$ .

### B. The binding energy

If  $\Psi_p^D$  denotes the normalized plane wave solution of Eq. (2.5) with momentum  $p$ , the potential energy of a nucleon with momentum  $p$  is equal to

$$\begin{aligned} \mathfrak{K}(p) &= \langle \Psi_p^D | U_0 + \beta U_s | \Psi_p^D \rangle \\ &= U_0 + U_s m^* (p^2 + m^{*2})^{-1/2}, \end{aligned} \quad (3.14)$$

where the effective mass  $m^*$  is defined by Eq. (3.6). The kinetic plus rest mass energy reads

$$\begin{aligned} \mathfrak{K}(p) &= \langle \Psi_p^D | \vec{\alpha} \cdot \vec{p} + \beta m | \Psi_p^D \rangle \\ &= (mm^* + p^2)(p^2 + m^{*2})^{-1/2}. \end{aligned} \quad (3.15)$$

The average total energy per nucleon of the nuclear matter ground state is given by

$$m + B/A = 3k_F^{-3} \int_0^{k_F} [\mathfrak{K}(p) + \frac{1}{2}u(p)] p^2 dp \quad (3.16a)$$

$$\begin{aligned} &= \frac{1}{2}U_0 - \frac{1}{2}U_s \frac{3m^*}{k_F^3} \\ &\quad \times \int_0^{k_F} \frac{p^2 dp}{(p^2 + m^{*2})^{1/2}} + \frac{3}{k_F^3} \\ &\quad \times \int_0^{k_F} p^2 (p^2 + m^{*2})^{1/2} dp. \end{aligned} \quad (3.16b)$$

From Eqs. (2.3) and (2.6)–(2.9), we find

$$\rho = \frac{2}{3\pi^2} k_F^3, \quad (3.17a)$$

$$\rho_s = \frac{4}{(2\pi)^3} \int_0^{k_F} \frac{m^*}{[p^2 + (m^*)^2]^{1/2}} d^3p, \quad (3.17b)$$

$$U_0 = \rho(g_\omega^2/m_\omega^2 + g_\phi^2/m_\phi^2), \quad (3.18)$$

$$U_s = -\rho_s g_\sigma^2/m_\sigma^2. \quad (3.19)$$

We note that in the present case of infinite nuclear matter the quantities  $U_0$  and  $U_s$  are independent of the cutoff energies  $\Lambda_i$ . By substituting the expressions (3.18) and (3.19) in Eq. (3.16b), it can be checked that one recovers Eq. (3.45) of Ref. 13. The relationship between the present notation and that of Ref. 13 is given by

$$c_s^2 = m^2 g_\sigma^2/m_\sigma^2, \quad c_v^2 = m^2 (g_\omega^2/m_\omega^2 + g_\phi^2/m_\phi^2). \quad (3.20)$$

### C. Input

Unless otherwise specified, our input is identical to that used by Brockmann<sup>22</sup> in his description of nuclear ground states. The meson parameters are the same as in the one-boson exchange potential of Erkelenz, Holinde, and Machleidt,<sup>37,38</sup> namely

$$m_\sigma = 550 \text{ MeV}, \quad g_\sigma^2/4\pi = 6.57, \quad \Lambda_\sigma = 1530 \text{ MeV}, \quad (3.21a)$$

$$m_\omega = 782.8 \text{ MeV}, \quad g_\omega^2/4\pi = 9.25, \quad \Lambda_\omega = 1530 \text{ MeV}, \quad (3.21b)$$

$$m_\phi = 1020 \text{ MeV}, \quad g_\phi^2/4\pi = 0.86, \quad \Lambda_\phi = 1530 \text{ MeV}. \quad (3.21c)$$

The corresponding constants (3.20) are

$$c_s^2 = 240.1, \quad c_v^2 = 176.1. \quad (3.22)$$

In the following, we shall occasionally neglect the

contribution of the  $\phi$  meson for simplicity. The corresponding coupling constants are

$$c_s^2 = 240.1, \quad c_v^2 = 166.9. \quad (3.23)$$

In his pioneering paper, Walecka<sup>13</sup> chose the values

$$c_s^2 = 266.9, \quad c_v^2 = 195.7. \quad (3.24)$$

#### D. Numerical results

In Fig. 1, we represent the dependence upon the Fermi momentum  $k_F$  of the average binding energy per nucleon, as calculated from the Hartree approximation (3.16b). The full curve corresponds to the exchange of mesons  $\sigma$  and  $\omega$  only; its minimum lies at  $k_F^{(0)} = 1.51 \text{ fm}^{-1}$ ,  $B/A = -21.6 \text{ MeV}$ . The dashed curve corresponds to the exchange of  $\sigma$ ,  $\omega$ , and  $\phi$  mesons; its saturation point lies at  $k_F^{(0)} = 1.45 \text{ fm}^{-1}$ ,  $B/A = -13 \text{ MeV}$ . The fact that the calculated  $k_F^{(0)}$  is larger than the empirical value ( $k_F^{(0)} = 1.36 \text{ fm}^{-1}$ ) suggests that in finite nuclei the calculated root mean square radius of the density will be smaller than the experimental value. This will be confirmed in Sec. IV A.

In Fig. 2, we show the energy dependence of the Schrödinger-equivalent potential  $U_e$ , Eq. (3.4), for  $k_F = 1.35 \text{ fm}^{-1}$  and  $k_F = 1.10 \text{ fm}^{-1}$ . The potential  $U_e(\epsilon)$  changes sign at  $\epsilon = 190 \text{ MeV}$  for  $k_F = 1.35 \text{ fm}^{-1}$ , while it becomes repulsive at  $\epsilon = 259 \text{ MeV}$  for the Fermi momentum  $k_F = 1.10 \text{ fm}^{-1}$ . We note that the two curves intersect. This feature

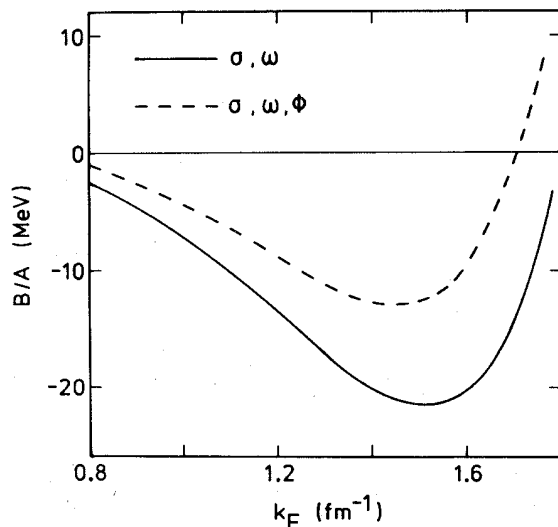


FIG. 1. Dependence upon the Fermi momentum  $k_F$  of the average binding energy per nucleon, as calculated from the relativistic Hartree approximation (3.16b). The full curve takes into account the exchange of  $\sigma$  and  $\omega$  mesons, and the dashed curve the exchange of  $\sigma$ ,  $\omega$ , and  $\phi$  mesons, with the parameter values (3.22) and (3.23), respectively.

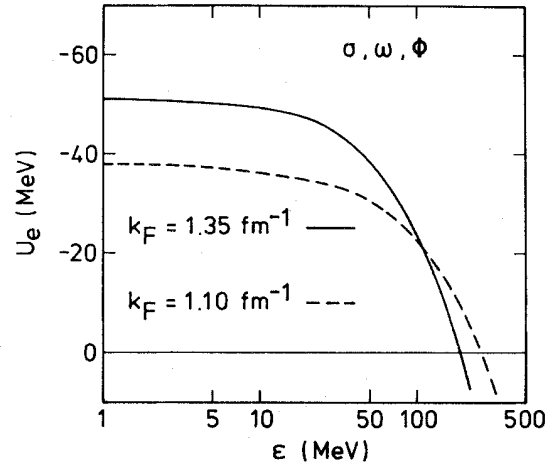


FIG. 2. Dependence upon the energy  $\epsilon$  of the Schrödinger-equivalent potential  $U_e$ , Eq. (3.4), in infinite nuclear matter with the Fermi momentum  $1.35 \text{ fm}^{-1}$  (full curve) and  $1.10 \text{ fm}^{-1}$  (dashed curve). The exchange of  $\sigma$ ,  $\omega$ , and  $\phi$  mesons is included.

will be discussed in detail in Sec. IV D. It is also encountered in a Brueckner-Hartree-Fock calculation based on Reid's hard core nucleon-nucleon interaction.<sup>46</sup>

The Fermi momentum  $k_F = 1.35 \text{ fm}^{-1}$  corresponds to the central density of medium-weight and heavy nuclei. In Fig. 3, we compare empirical depths of the optical-model potential of  $^{40}\text{Ca}$  with the values of  $U_e(\epsilon)$  for infinite nuclear matter with  $k_F = 1.35 \text{ fm}^{-1}$ . The fair agreement indicates that the present relativistic Hartree model reproduces the low-energy behavior of the optical-model potential. The dependence of  $U_e(\epsilon)$  is linear. It is customary to characterize this ener-

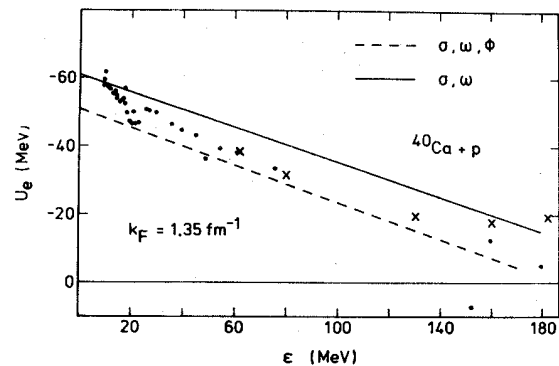


FIG. 3. The crosses and the dots show empirical potential depths determined from the analysis of proton scattering by  $^{40}\text{Ca}$ , carried out in Refs. 36 and 47, respectively. The straight lines represent calculated depths for infinite nuclear matter with  $k_F = 1.35 \text{ fm}^{-1}$ . The dashed line corresponds to  $\sigma$ ,  $\omega$ , and  $\phi$  exchange, and the full line to  $\sigma$  and  $\omega$  exchange.

gy dependence by the following quantity  $\bar{m}$ , which is called the "effective mass" in the field of nuclear spectroscopy or of nuclear reaction theory:

$$\frac{\bar{m}}{m} = 1 - \frac{dU_\epsilon}{d\epsilon} = 1 - U_0/m. \quad (3.25)$$

For  $k_F = 1.35 \text{ fm}^{-1}$ , we find  $\bar{m}/m = 0.73$ . This result is close to the empirical value, which is 0.78 for  $0 < \epsilon < 100 \text{ MeV}$ . This good agreement appears to be slightly at variance with the smaller value of the effective mass obtained by Duerr<sup>4</sup> and by Walecka.<sup>13</sup> However, the effective mass dealt with by these authors is the quantity defined by Eq. (3.6). The origin of the expression effective mass coined for  $m^*$  in Refs. 4 and 13 is apparent from Eq. (3.10a). For  $k_F = 1.35 \text{ fm}^{-1}$ , one has  $m^*/m = 0.65$  for the input parameters (3.21a)–(3.21c). In the case of Walecka's parameters (3.24), one finds  $\bar{m}/m = 0.70$  and  $m^*/m = 0.61$ . We note that Arnold and Clark<sup>10</sup> recently introduced yet another effective mass, namely the quantity  $M^*$  defined by

$$\frac{M^*}{m} = 1 - \frac{U_0 - U_s}{2m} = \frac{\bar{m} + m^*}{2m}. \quad (3.26)$$

In the past, some authors<sup>4,7</sup> had worked within the framework of the Foldy-Wouthuysen approximation (3.9) or of the low-energy approximation (3.11). In order to test the accuracy of these approximations, we compare them with the exact result in Fig. 4 for  $k_F = 1.35 \text{ fm}^{-1}$  and in the case of the  $\sigma, \omega$  model. We see that the Foldy-Wouthuysen approximation (3.9) is not accurate. This reflects the fact that the inequalities (2.22) are

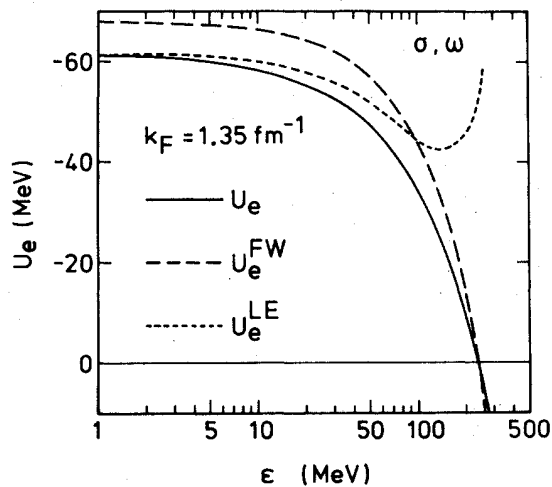


FIG. 4. Comparison between the exact value of  $U_\epsilon$  [Eq. (3.7)] (full curve), the Foldy-Wouthuysen approximation Eq. (3.9) (long dashes), and the low-energy approximation (3.11) (short dashes) in the case of infinite nuclear matter at  $k_F = 1.35 \text{ fm}^{-1}$ , for the  $\sigma, \omega$  model.

not well fulfilled in the present case. This is due to the fact that the ratios  $U_s/m$  and  $U_0/m$  are not small. The low-energy approximation (3.11) is reasonably accurate only for  $\epsilon$  smaller than several tens MeV.

#### IV. FINITE NUCLEI: $^{16}\text{O}$ AND $^{40}\text{Ca}$

##### A. Density distribution

The full curves in Figs. 5 and 6 represent the baryon density of  $^{16}\text{O}$  and of  $^{40}\text{Ca}$ , as calculated from the exchange of  $\sigma, \omega$ , and  $\phi$  mesons.<sup>48</sup> The shape of  $\rho(r)$  in the case of  $^{16}\text{O}$  is typical of a Hartree approximation. Indeed, it is closely fitted by the formula

$$\rho_{\text{HO}}(r) = \rho_0 \left( 1 + 2 \frac{r^2}{a^2} \right) \exp \left( -\frac{r^2}{a^2} \right), \quad (4.1)$$

which is the form derived for the density of  $^{16}\text{O}$  in a nonrelativistic independent particle model with harmonic oscillator wave functions. The dashed curve in Fig. 5 represents the function  $\rho_{\text{HO}}(r)$  with the following parameters:  $\rho_0 = 0.207 \text{ nucleon fm}^{-3}$ ,  $a = 1.55 \text{ fm}$ . In the nuclear interior, the calculated density distribution of  $^{40}\text{Ca}$  is flatter than in the case of  $^{16}\text{O}$ . The dashed curve in Fig. 6 represents the Fermi distribution

$$\rho_F(r) = \frac{\rho_0}{1 + \exp(r-R)/a)}, \quad (4.2)$$

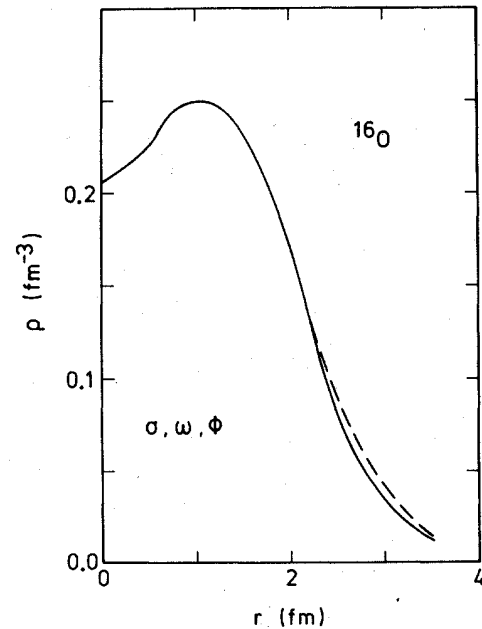


FIG. 5. The full curve represents the baryon density of  $^{16}\text{O}$  as calculated from the relativistic Hartree approximation (Ref. 48). The dashed curve corresponds to a fit with expression (4.1).

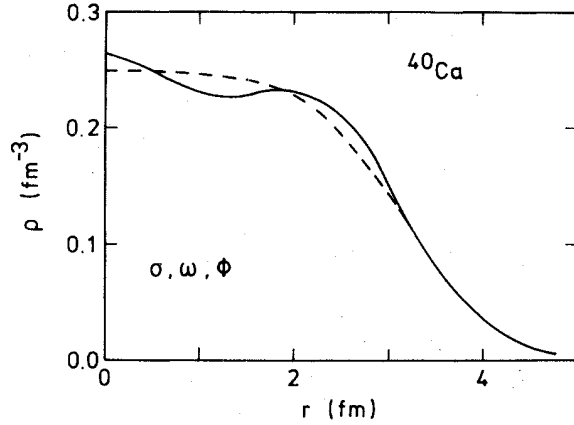


FIG. 6. The full curve represents the baryon density of  $^{40}\text{Ca}$  as calculated from the relativistic Hartree approximation (Ref. 48). The dashed curve corresponds to a fit with expression (4.2).

with  $\rho_0 = 0.25$  nucleon  $\text{fm}^{-3}$ ,  $R = 0.92 A^{1/3}$ , and  $a = 0.47$  fm. For semiquantitative purposes, it is thus justified to consider  $^{16}\text{O}$  as a typical light nucleus, and  $^{40}\text{Ca}$  as a representative of a medium-weight of heavy nucleus.

The calculated root mean square radius of  $^{16}\text{O}$  is equal to 2.30 fm and that of  $^{40}\text{Ca}$  to 2.97 fm. These values are rather smaller than the experimental ones, which are equal to 2.45 fm (Ref. 49) and to 3.48 fm (Ref. 50), respectively. This reflects the fact that the calculated saturation density of nuclear matter is too large and entails that the calculated central density is also too large. This defect of the present model will have to be taken into account when comparing our results with empirical values.

#### B. Static central potentials

For simplicity, it will often be convenient to drop the contribution of the  $\phi$  meson to the fourth component  $U_0(r)$  of the vector part of the Hartree-Dirac field. Accordingly, we write

$$U_0(r) = U_0^\omega(r) + U_0^\phi(r), \quad (4.3)$$

where [see Eq. (2.7)]

$$U_0^\omega(r) = \int \rho(r') \mathcal{U}_\omega(|\vec{r} - \vec{r}'|) d^3r'. \quad (4.4)$$

The values of  $U_0^\omega(r)$  and of  $U_s(r)$  are shown in Figs. 7 and 8, in the case of  $^{16}\text{O}$  and of  $^{40}\text{Ca}$ , respectively. The scales have been adjusted in such a way that the ordinate of  $U_0^\omega(0)$  coincides with that of  $U_s(0)$ . We note that  $U_0^\omega(r)$  and  $U_s(r)$  have approximately the same shape down to  $\frac{2}{3}$  of the central value. One has

$$U_s(r) \approx -1.3U_0(r), \quad r < r_m, \quad (4.5)$$

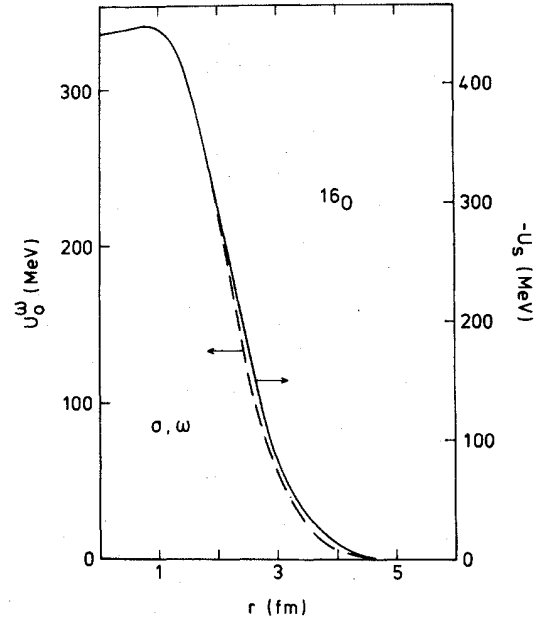


FIG. 7. Comparison between the shapes of  $U_0^\omega(r)$  (dashed curve, left-hand scale) and of  $U_s(r)$  (full curve, right-hand scale) in the case of  $^{16}\text{O}$ .

with  $r_m \approx 2$  fm in the case of  $^{16}\text{O}$  and  $r_m \approx 3$  fm in the case of  $^{40}\text{Ca}$ . This property will be used in Sec. IV D. For  $r > r_m$ ,  $U_s(r)$  extends beyond  $U_0(r)$ . This is mainly due to the fact that the scalar meson is lighter than the vector meson. The effect of this mass difference is partly compensated by the fact that the range of the scalar den-

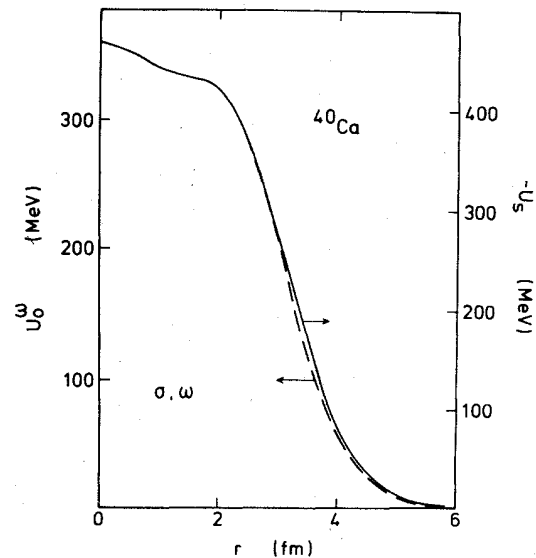


FIG. 8. Comparison between the shapes of  $U_0^\omega(r)$  (dashed curve, left-hand scale) and of  $U_s(r)$  (full curve, right-hand scale) in the case of  $^{40}\text{Ca}$ .



sity is slightly smaller than that of the baryonic density.

### C. Schrödinger-equivalent potential

The central part of the Schrödinger-equivalent potential is given by Eq. (2.13). Let us for simplicity set  $g_\sigma^2 = 0$  and denote  $U_\sigma^{\sigma+\omega}(r; \epsilon)$  the corresponding value of  $U_\sigma(r; \epsilon)$ . We usually illustrate the discussion by the case of  $^{40}\text{Ca}$ . Similar results hold for  $^{16}\text{O}$ . The full curve in Fig. 9 represents the radial dependence of  $U_\sigma^{\sigma+\omega}(r; 0)$ ; the dashed curve is a Woods-Saxon well with the following parameters ( $R = r_0 A^{1/3}$ ):

$$V_0 = 61.8 \text{ MeV}, \quad r_0 = 1.09 \text{ fm}, \quad a = 0.54 \text{ fm}. \quad (4.6)$$

The dash-and-dot curve represents the quantity  $U_\sigma^\omega(r) + U_s(r)$ ; the difference between this curve and the full curve illustrates the importance of the quadratic terms on the right-hand side of Eq. (2.13).

In Fig. 10, we show the value of  $U_\sigma^{\sigma+\omega}(r; \epsilon)$  at the energies  $\epsilon = 0, 150, 300,$  and  $450$  MeV. We note that  $U_\sigma(r; \epsilon)$  changes sign at a much lower energy at the nuclear center than at the nuclear surface. This reflects the intersection of the two curves shown in Fig. 2. As a consequence, the Schrödinger-equivalent potential acquires an attractive pocket at the nuclear surface in the intermediate energy domain.<sup>11</sup> The origin of this wine-bottle bottom shape will be discussed in Sec. IV D.

We turn to a comparison between the relativistic Hartree model and the empirical data. Figure 3 already indicated that the agreement is fairly satisfactory. It is known, however, that the depth of the optical-model potential is not well determined by the analysis of the data, and that the

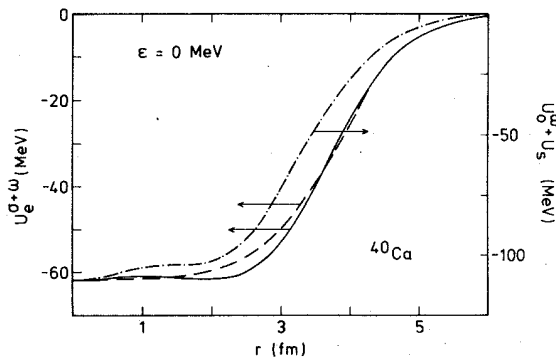


FIG. 9. The full curve shows the radial dependence of  $U_\sigma^{\sigma+\omega}(r; \epsilon)$  for  $\epsilon = 0$  MeV, in the case of  $^{40}\text{Ca}$ . The long dashed represent a Woods-Saxon potential, with the parameters (4.6). The dash-and-dot curve represents the sum  $U_\sigma^\omega(r) + U_s(r)$  (right-hand scale).

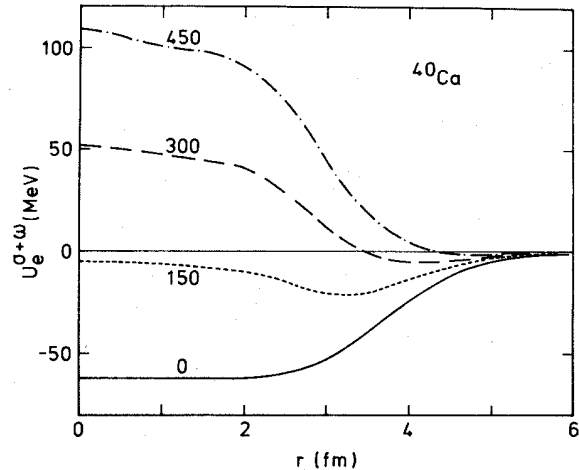


FIG. 10. Schrödinger-equivalent potential  $U_\sigma^{\sigma+\omega}(r; \epsilon)$  in the case of  $^{40}\text{Ca}$ , for  $\epsilon = 0, 150, 300,$  and  $450$  MeV.

differential cross sections are mainly sensitive to the volume integral per nucleon of the potential well, namely,

$$J_{U_\sigma}/A = 4\pi A^{-1} \int U_\sigma(r) r^2 dr. \quad (4.7)$$

The dots in Figs. 11 and 12 represent empirical values of  $J_{U_\sigma}/A$ , obtained from analyses of proton scattering by  $^{16}\text{O}$  and  $^{40}\text{Ca}$ , respectively. The theoretical results are represented by the full curve in the  $\sigma, \omega$  model [Eq. (3.23)] and by the dashed curve in the  $\sigma, \omega, \phi$  model [Eq. (3.22)]. In the case of  $^{16}\text{O}$ , the volume integral changes sign at 290 MeV in the  $\sigma, \omega$  model and at 238 MeV in the

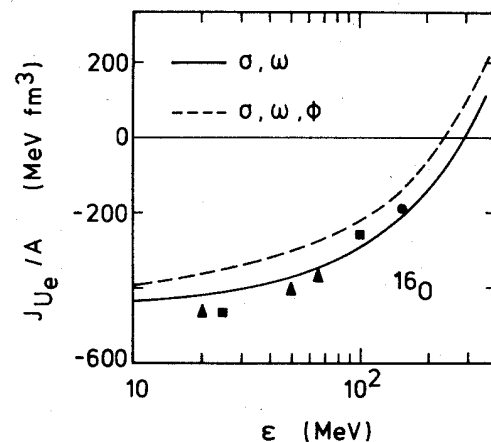


FIG. 11. Comparison between calculated and empirical values of the volume integral per nucleon of the optical-model potential of  $^{16}\text{O}$ . The squares (Ref. 51), triangles (Ref. 52), and the full dot (Ref. 53) have been obtained from analyses of proton scattering. The full line corresponds to  $\sigma, \omega$  exchange and the dashed line to  $\sigma, \omega, \phi$  exchange.

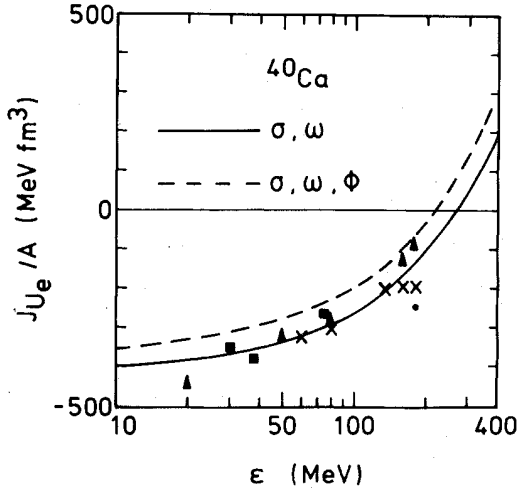


FIG. 12. Comparison between calculated and empirical values of the volume integral per nucleon of the optical-model potential of  $^{40}\text{Ca}$ . The squares (Ref. 51), triangles (Ref. 52), crosses (Ref. 36), and dot (Ref. 36) have been obtained from analyses of proton scattering. The full line corresponds to  $\sigma$ ,  $\omega$  exchange and the dashed line to  $\sigma$ ,  $\omega$ ,  $\phi$  exchange.

$\sigma$ ,  $\omega$ ,  $\phi$  model. In the case of  $^{40}\text{Ca}$ , these energies become 270 and 220 MeV, respectively. These energies are significantly larger than the energy at which the central value changes sign. This is due to the fact that the Schrödinger-equivalent potential  $U_e(r; \epsilon)$  has a wine-bottle bottom shape at intermediate energy.

The mean square radius of the potential well is defined by

$$\langle r^2(U_e) \rangle = \left[ \int r^4 U_e(r; \epsilon) dr \right] \left[ \int r^2 U_e(r; \epsilon) dr \right]^{-1}. \quad (4.8)$$

Since the shape of  $U_e(r; \epsilon)$  depends on energy,  $\langle r^2(U_e) \rangle$  is an energy-dependent quantity. Furthermore, the calculated value of  $\langle r^2(U_e) \rangle$  becomes singular at the energy at which the volume integral  $J_{U_e}$  changes sign. This is illustrated by the full curve in Fig. 13 in the case of  $^{40}\text{Ca}$  and of the  $\sigma$ ,  $\omega$ , model. At intermediate energy, the calculated value of the root mean square radius is very sensitive to the location of the singularity. This suggests that we consider the following quantity:

$$\langle r^2(|U_e|) \rangle = \left[ \int r^4 |U_e(r; \epsilon)| dr \right] \left[ \int r^2 |U_e(r; \epsilon)| dr \right]^{-1}. \quad (4.9)$$

It is represented by the long dashes in Fig. 13. We note that the quantities (4.8) and (4.9) are not well determined by the empirical analyses if one restricts the empirical form factor of  $U_e(r; \epsilon)$  to

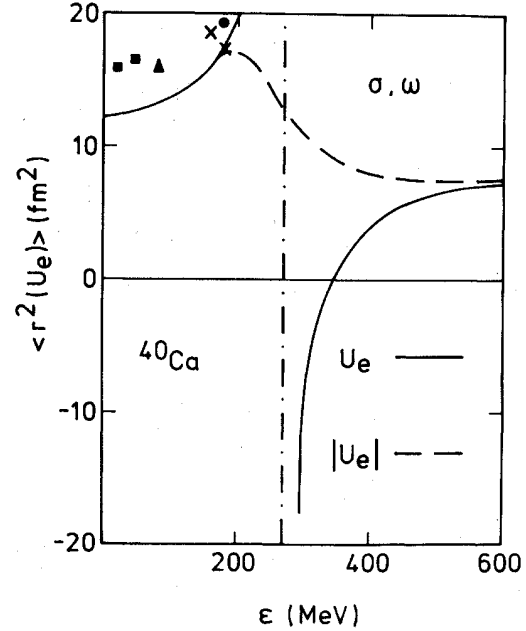


FIG. 13. The full curve represents the mean square radius (4.8) of the Schrödinger-equivalent potential in the case of  $^{40}\text{Ca}$  and of the  $\sigma$ ,  $\omega$  model; it is singular at the energy, indicated by the dash-and-dot line, where the volume integral changes sign. The quantity  $\langle r^2(|U_e|) \rangle$  defined by Eq. (4.9) is represented by long dashes. The empirical values are taken from Refs. 51 (squares), 52 (triangle), and 36 (crosses and full dot).

a Woods-Saxon shape. Nevertheless, it appears that the calculated values are significantly smaller than the empirical ones. This discrepancy reflects the fact that the calculated mean square radius of the baryonic density is too small.

One might conclude from Figs. 11 and 12 that the  $\sigma$ ,  $\omega$  model is in better agreement with experiment than the  $\sigma$ ,  $\omega$ ,  $\phi$  model. However, this impression would be ill-founded. Indeed, the main reason why the  $\sigma$ ,  $\omega$ ,  $\phi$  model yields too small (in absolute magnitude) values of  $J_{U_e}/A$  is that the calculated root mean square radius of the density and of the potential is too small. This is exhibited in Fig. 14. There, we compare the empirical values of the volume integral per nucleon of the optical model of  $^{208}\text{Pb}$  with theoretical results obtained from the following local density approximation. We take the density  $\rho(r)$  from experiment, more explicitly from Eq. (2.29) of Ref. 54. Then, we assume that for each value of  $r$  the potentials  $U_0(r)$  and  $U_s(r)$  are given by the formulas

$$U_0(r) = \rho(r)c_v^2/m^2, \quad U_s(r) = -\rho_s(r)c_s^2/m^2, \quad (4.10)$$

where the ratio  $\rho(r)/\rho_s(r)$  is taken the same as in

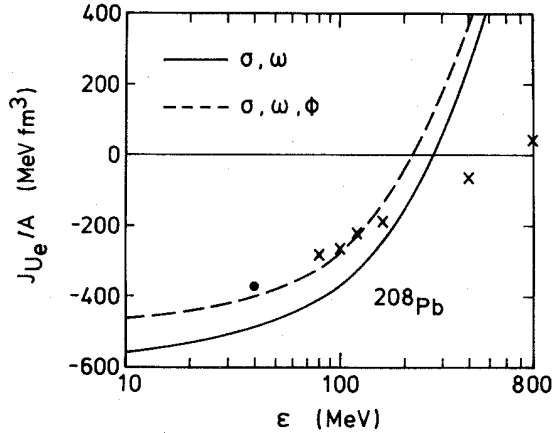


FIG. 14. Dependence upon energy of the volume integral per nucleon of the optical-model potential of  $^{208}\text{Pb}$ , as calculated from the local density approximation (4.10). The full line corresponds to the  $\sigma, \omega$  model and the dashed curve to the exchange of  $\sigma, \omega$ , and  $\phi$  mesons. The empirical values are taken from Refs. 36 (crosses) and 35 (dot).

nuclear matter at the local density  $\rho(r)$ , while the constants  $c_v^2$  and  $c_s^2$  are taken from Eqs. (3.22) and (3.23). Figure 14 shows that the  $\sigma, \omega, \phi$  model now yields better agreement with empirical values below 200 MeV. At higher energies, both the  $\sigma, \omega$  and the  $\sigma, \omega, \phi$  models yield too much repulsion.

#### D. Wine-bottle bottom shape

At intermediate energy there exists a nearly complete cancellation between the attractive and repulsive components of the optical-model potential. In the present model, these components are ascribed to the exchange of scalar and of vector mesons, respectively. Hence, the delicate balance between these two contributions can best be investigated at intermediate energy. One of the striking features of the results described in the preceding sections is that at intermediate energy the calculated Schrödinger-equivalent potential has an attractive pocket at the nuclear surface. In the present section we investigate the origin of this wine-bottle bottom shape and we compare this result with experimental evidence.

The wine-bottle bottom shape is displayed in Figs. 15 and 16, at the energies where the Schrödinger-equivalent potential changes sign at the nuclear center in the  $\sigma, \omega$  and in the  $\sigma, \omega, \phi$  models. Except for energy shifts, the phenomenon is quite similar in both models. Therefore, we only consider the  $\sigma, \omega$  model in the following discussion, and we drop the upper indices  $\sigma$  and  $\omega$ .

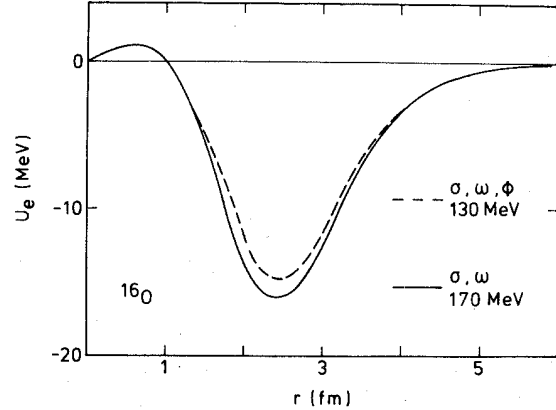


FIG. 15. Schrödinger-equivalent potential  $U_e(r)$  for  $^{16}\text{O}$  at the energy  $\epsilon_0(0)$  at which it vanishes at  $r=0$  fm. The full curve corresponds to the  $\sigma, \omega$  model [ $\epsilon_0(0)=170$  MeV] and the long dashed to the exchange of  $\sigma, \omega$ , and  $\phi$  mesons [ $\epsilon_0(0)=130$  MeV].

Let us write Eq. (2.13) in the following form:

$$U_e(r; \epsilon) = U_e(r; 0) + \frac{\epsilon}{m} U_0(r), \quad (4.11)$$

where the energy-independent part is

$$U_e(r; 0) = [U_s(r) + U_0(r)] \frac{M^*(r)}{m}. \quad (4.12)$$

Here,  $M^*(r)$  is the  $r$ -dependent average effective mass defined by Eq. (3.26). In Fig. 17, we compare the shape of  $U_e(r; 0)$  with that of  $U_0(r)$ . We note in particular that the range of the repulsive and energy-dependent component  $(\epsilon/m)U_0(r)$  of  $U_e(r; \epsilon)$  is significantly smaller than that of  $U_e(r; 0)$ . That is why  $U_e(r; \epsilon)$  has an attractive surface pocket at the energy  $\epsilon_0(0)$  at which  $U_e[0; \epsilon_0(0)] = 0$ .

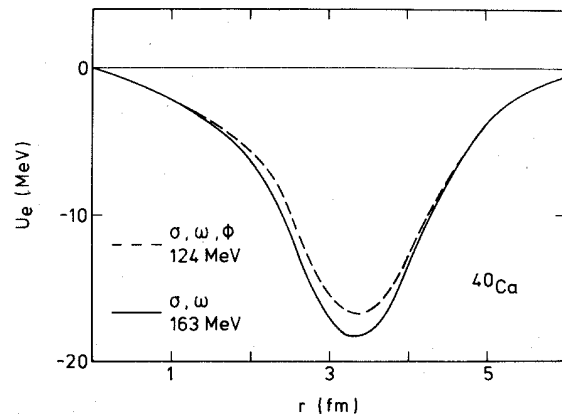


FIG. 16. Schrödinger-equivalent potential  $U_e(r)$  for  $^{40}\text{Ca}$  at the energy  $\epsilon_0(0)$  at which it vanishes at  $r=0$  fm. The full curve corresponds to the  $\sigma, \omega$  model [ $\epsilon_0(0)=163$  MeV] and the long dashes to the exchange of  $\sigma, \omega$ , and  $\phi$  mesons [ $\epsilon_0(0)=124$  MeV].

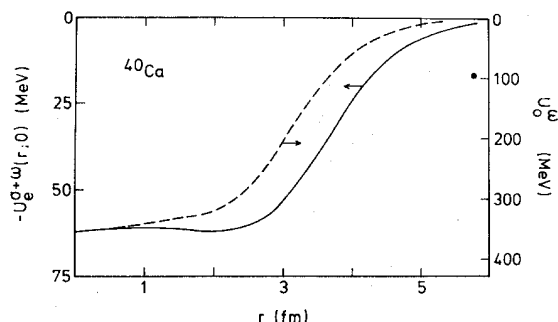


FIG. 17. Radial dependence of the quantity  $U_e(r; 0)$  (full curve) and of the coefficient  $U_0(r)$  of  $\epsilon/m$  in Eq. (4.11) (long dashes) in the case of  $^{40}\text{Ca}$  and of the  $\sigma, \omega$  model.

We now discuss the origin of the fact that the range of  $U_0(r)$  is smaller than that of  $U_e(r; 0)$ . We first recall that Figs. 7 and 8 show that  $U_0(r)$  and  $U_s(r)$  have very nearly the same shape for  $r < r_m$ , with  $r_m \approx 2$  fm in the case of  $^{16}\text{O}$  and  $r_m \approx 3$  fm in the case of  $^{40}\text{Ca}$ . Since the wine-bottle bottom shape is already quite pronounced for  $r$  smaller than  $r_m$ , we conclude that its main origin does not lie in a shape difference between  $U_0(r)$  and  $U_s(r)$ . Let us therefore assume that the following relation holds for all  $r$ :

$$U_s(r) \approx -\frac{4}{3} U_0(r). \quad (4.13)$$

Within this simplified model, Eqs. (4.11) and (4.12) yield

$$U_e(r; \epsilon) \approx -\frac{1}{3} U_0(r) \left[ \frac{M^*(r)}{m} - 3 \frac{\epsilon}{m} \right], \quad (4.14)$$

$$\frac{M^*(r)}{m} \approx 1 - \frac{7}{3} \frac{U_0(r)}{2m}. \quad (4.15)$$

The energy  $\epsilon_0(r)$  at which  $U_e^{\sigma, \omega}(r; \epsilon)$  vanishes is then given by

$$\epsilon_0(r) \approx \frac{m}{3} \frac{M^*(r)}{m} \approx 313 \frac{M^*(r)}{m} \text{ MeV}. \quad (4.16)$$

The quantity  $M^*(r)/m$  as approximated by Eq. (4.15) is represented in Fig. 18 in the case of  $^{40}\text{Ca}$ ; it is practically indistinguishable from its exact value given by Eq. (3.26). The ratio  $M^*(r)/m$  varies from 0.56 at the nuclear center to unity at the nuclear tail. Accordingly, Eq. (4.16) shows that  $\epsilon_0(r)$  varies from approximately 175 MeV at the nuclear center to 313 MeV at the nuclear tail. This discussion shows that the main origin of the longer range of  $U_e(r; 0)$  compared to that of  $U_0(r)$  lies in the radial dependence of the average effective mass  $M^*(r)$ , which reflects the presence of the quadratic terms on the right-hand side of Eq. (2.13).

Humphreys<sup>9</sup> had proposed that the origin of the wine-bottle bottom shape lies in the fact that the

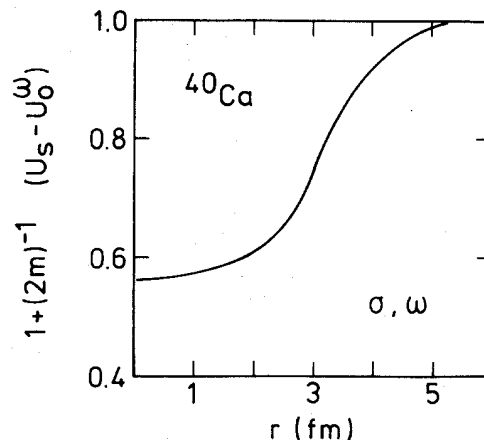


FIG. 18. Plot of the radial dependence of the average effective mass  $M^*(r)/m$  [Eq. (3.26)], as approximated by Eq. (4.15), in the case of  $^{40}\text{Ca}$  and of the  $\sigma, \omega$  model.

root mean square radius of  $U_0(r)$  is smaller than that of  $U_s(r)$ , because the mass of the vector meson is larger than that of the scalar meson. Although this mass difference contributes to the effect under discussion, especially above 313 MeV, it is not its sole cause. This is exhibited in Fig. 19 which shows that the wine-bottle bottom shape is already well-pronounced within the approximation (4.14). The difference in shape between  $U_s(r)$  and  $U_0(r)$  somewhat increases the size of the pocket, especially in the tail region. The mass difference is also responsible for the fact that the attractive dip persists at energies higher than 313 MeV, which is the energy at which the potential would become entirely repulsive if approximation (4.13) were correct for all values of  $r$ . We also note that Humphreys' model<sup>9</sup> involved intuitive arguments based on the Lorentz contraction of the source of scalar mesons. Humphreys

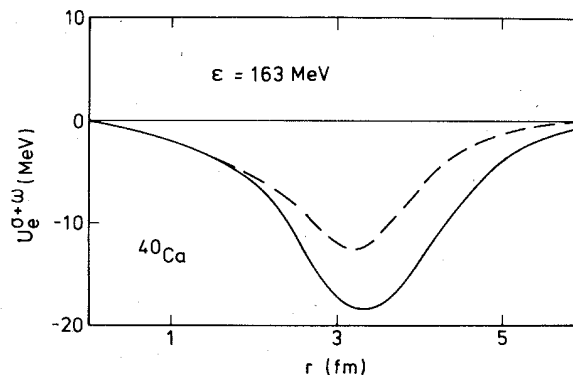


FIG. 19. Comparison between the exact value of the Schrödinger-equivalent potential of  $^{40}\text{Ca}$  at 163 MeV in the  $\sigma, \omega$  model (full curve) and the approximation defined by Eqs. (4.14) and (4.15) (dashed curve).

wrote

$$U_e(r) = U_0 + \frac{m}{m + \epsilon} U_s \approx \left(1 - \frac{1}{2} \frac{k_\infty^2}{m^2}\right) U_s(r) + U_0(r). \quad (4.17)$$

We recognize the nonrelativistic limit of expression (3.9); this is quite inaccurate as we showed in Fig. 4.

We now turn to a discussion of whether a wine-bottle bottom shape for the optical-model potential may be required in order to fit the experimental data at intermediate energy. In an early paper, Elton<sup>55</sup> analyzed the elastic scattering, polarization, and reaction cross sections for 180 MeV protons scattered by <sup>56</sup>Fe. He found convincing empirical evidence that the real part of the optical-model potential has an attractive surface pocket; his analysis did not enable him to find the amount by which  $U_e(r)$  is repulsive in the inner region. In Fig. 20, we compare the phenomenological potential obtained by Elton<sup>55</sup> with a theoretical Schrödinger-equivalent potential calculated within the framework of the local density approximation (4.10). The semiquantitative agreement between Elton's empirical potential and the calculated potential is quite striking. For comparison, we also show in Fig. 20 the optical-model potential

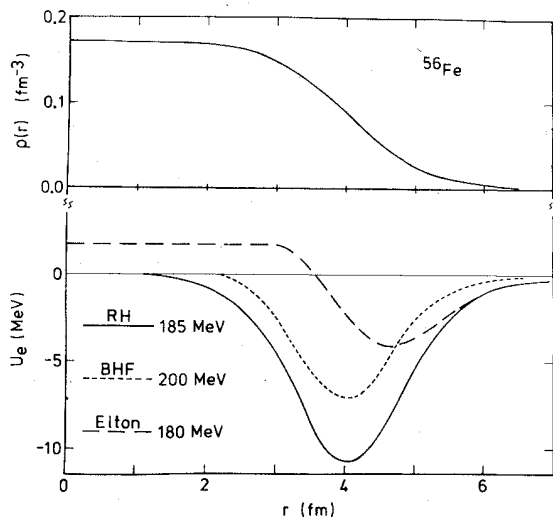


FIG. 20. The dashed curve represents the empirical potential determined by Elton (Ref. 55) from the analysis of proton scattering by <sup>56</sup>Fe at 180 MeV. The full curve shows the Schrödinger-equivalent potential as calculated from the local density approximation defined by Eq. (4.14), in the  $\sigma$ ,  $\omega$ ,  $\phi$  model. The short dashes represent the optical-model potential as calculated from the Brueckner-Hartree-Fock approximation with Reid's hard core nucleon-nucleon interaction (Ref. 56). The upper part of the figure gives the assumed density  $\rho(r)$  (Ref. 54).

as computed from the Brueckner-Hartree-Fock approximation based on Reid's hard core nucleon-nucleon interaction.<sup>56</sup> Finally, we note that a recent analysis<sup>57</sup> of differential cross sections of protons by <sup>40</sup>Ca at 181 MeV appears to confirm the existence of a wine-bottle bottom shape for the average potential.

An interesting consequence of the wine-bottle bottom shape is that there exists an energy domain in which the mean square radius of the potential is negative. This occurs because in the numerator of the defining expression (4.8) the surface region is weighed more heavily than in the denominator. This change of the sign of  $\langle r^2(U_e) \rangle$  could be detected empirically only if the possibility that wine-bottle bottom shapes can occur were included in the phenomenological analyses. In practice, one chooses *a priori*  $U_e(r; \epsilon)$  to be a Woods-Saxon potential, in which case  $\langle r^2(U_e) \rangle$  is always positive. However, if the rendering of the data really requires a wine-bottle bottom shape for  $U_e(r; \epsilon)$ , the quality of the standard analyses should become poorer at intermediate energy, or else the energy dependence of the parameters should show unexpected changes. Some indications exist that this is happening indeed. For instance, in a recent analysis of new data of proton elastic scattering by Pb, Schwandt and collaborators<sup>58</sup> found that the root mean square radius of the phenomenological potential drops by as much as ten per cent between 200 and 400 MeV.

#### E. Spin-orbit potential

One of the merits of the relativistic Hartree model is that it automatically yields a strong spin-orbit potential.<sup>9,10,16,19,21,26,30,32,59-61</sup> This potential is given by Eq. (2.14), which we write in the form

$$U_{so}(r; \epsilon) = -v_s f(0; \epsilon) (m_\pi)^{-2} \frac{d}{dr} \left[ \frac{f(r; \epsilon)}{f(0; \epsilon)} \right], \quad (4.18)$$

with

$$f(r; \epsilon) = \ln \{ [2m + \epsilon + U_s(r) - U_0(r)] (2m + \epsilon)^{-1} \}, \quad (4.19)$$

and  $(m_\pi)^{-2} = 2 \text{ fm}^2$ ,  $v_s = 10.5 \text{ MeV}$ .

The quantity  $f(r; \epsilon)$  does not have the same radial dependence as  $U_e(r; \epsilon)$ . We showed in Sec. IVD that this is partly due to the presence of the quadratic term  $(2m)^{-1} [U_s^2(r) - U_0^2(r)]$  on the right-hand side of Eq. (2.13). In other words, the range of  $U_e(r; \epsilon)$  is significantly larger than that of  $f(r; \epsilon)$ , even if  $U_s(r)$  and  $U_0(r)$  have the same radial form factor. This geometrical feature appears to have been overlooked by Arnold and Clark,<sup>30</sup> who

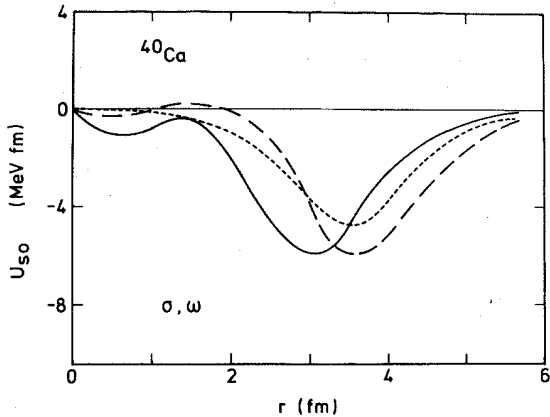


FIG. 21. The full curve represents the spin-orbit potential  $U_{so}(r; \epsilon)$  as calculated from Eq. (2.14) in the  $\sigma, \omega$  model, for  $^{40}\text{Ca}$  at  $\epsilon = 50$  MeV. The long dashes represent expression (4.18). The short dashes show the average of the empirical spin-orbit potentials found by van Oers (Ref. 47).

ascribe the difference

$$\delta^2 = \langle r^2(U_\sigma) \rangle - \langle r^2(f) \rangle \quad (4.20)$$

fully to the mass difference between scalar and vector mesons. Although this mass difference contributes to  $\delta^2$ , it does not play a more important role than the quadratic term. The latter significantly differs from zero because of the difference between the strengths  $g_\sigma^2/m_\sigma^2$  and  $g_\omega^2/m_\omega^2$ .

The full curve in Fig. 21 represents the value of  $U_{so}(r; \epsilon)$  at  $\epsilon = 50$  MeV in the case of  $^{40}\text{Ca}$  and of the  $\sigma, \omega$  model. The dashed curve shows the quantity

$$-V_{so} \left( \frac{\hbar}{m_\sigma c} \right)^2 \frac{d}{dr} \left[ \frac{U_\sigma(r)}{U_\sigma(0)} \right], \quad (4.21)$$

where the strength  $V_{so}$  has been chosen in such a way that the minimum of (4.21) has the same depth as that of  $U_{so}(r)$ . This yields  $V_{so} = 5.7$  MeV, which is in good agreement with the spin-orbit strength  $V_{so} = 6.2$  MeV of the empirical potential of Becchetti and Greenlees.<sup>62</sup> Fits of the polarization data for proton scattering have been performed by van Oers<sup>47</sup> for  $^{40}\text{Ca}$ , at a number of energies. The short dashes in Fig. 21 represent an average of these empirical potentials. We note the good agreement with the calculated value. One can also compare calculated and empirical values of the volume integral

$$J_{so}/A^{1/3} = A^{-1/3} \int \frac{1}{r} U_{so}(r; \epsilon) d^3r. \quad (4.22)$$

This is done in Fig. 22. We note that the empirical values of Nadasen *et al.*<sup>36</sup> seem to indicate a sizable decrease of  $|J_{so}|$  when  $\epsilon$  increases. In the

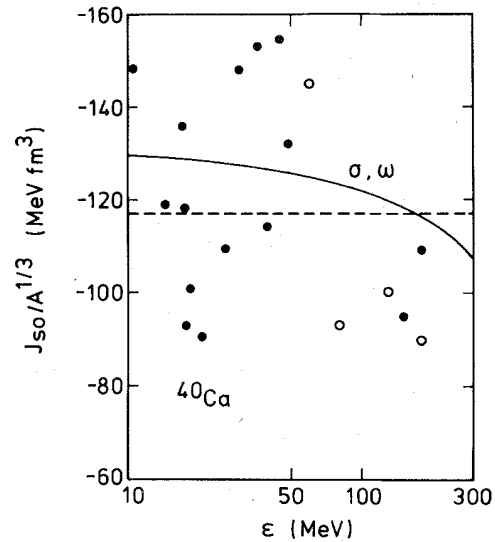


FIG. 22. Comparison between the volume integral (4.22) of the spin-orbit potential of  $^{40}\text{Ca}$  as calculated from the  $\sigma, \omega$  model (full curve) with the average of the empirical values determined by van Oers (Ref. 47) (short dashes). The full dots represent the empirical values of van Oers. The open dots correspond to the empirical values of Nadasen *et al.* (Ref. 36).

relativistic Hartree approximation, the decrease of  $|J_{so}|$  with increasing energy is very weak. The same holds true for the volume integral of the spin-orbit potentials calculated in the framework of the Brueckner-Hartree-Fock approximation<sup>63</sup> as well as in the framework of the multiple scattering expansion.<sup>64</sup> Hence, a major problem will arise if the existence of a significant decrease of  $|J_{so}|$  with increasing  $\epsilon$  is confirmed by more detailed analyses of experimental data.

## V. SUMMARY

The optical-model potential at positive energy has been investigated in the framework of the relativistic Hartree approximation. No parameter has been adjusted in our calculation. We adopted the same meson masses and coupling constants as Brockmann<sup>22</sup> in his recent study of nuclear ground states. In view of this, the comparison between the empirical values of the optical-model potential and the calculated potential is quite satisfactory. In order to perform this comparison, we constructed the Schrödinger-equivalent potential of the relativistic Hartree potential. Good agreement is obtained at low and at intermediate energy, for both the central and the spin-orbit components of the optical-model potential. The relationship between the relativistic Hartree potential and the Schrödinger-equivalent potential, and also between the present work and that of previous

authors,<sup>5-7,10,13</sup> has been illustrated in the simple case of infinite nuclear matter, where many relations take a transparent form.

One of the interesting features of the calculated Schrödinger-equivalent potential is that it has an attractive pocket at the nuclear surface. This wine-bottle bottom shape in particular is responsible for the fact that the volume integral of the potential changes sign at an energy which is much higher than the one at which the potential changes

sign at the nuclear center. Another consequence is that the root mean square radius displays a significant energy dependence at intermediate energy.

#### ACKNOWLEDGMENTS

We are very grateful to Dr. R. Brockmann for kindly having sent us the details of his results published in Ref. 22. Stimulating discussions or correspondence with G. E. Brown, B. C. Clark, and W. Weise are gratefully acknowledged.

- <sup>1</sup>C. Mahaux, in *Microscopic Optical Potentials*, edited by H. V. Von Geramb (Springer, Berlin, 1979), p. 1.
- <sup>2</sup>A. E. S. Green, in *The Nuclear Many-Body Problem*, edited by F. Calogero and C. Ciolfi degli Atti (Editrice Compositori, Bologna, 1973), p. 771.
- <sup>3</sup>M. H. Johnson and E. Teller, *Phys. Rev.* **98**, 783 (1955).
- <sup>4</sup>H. P. Duerr, *Phys. Rev.* **103**, 469 (1956).
- <sup>5</sup>H. P. Duerr, *Phys. Rev.* **109**, 117 (1958); **109**, 1347 (1958).
- <sup>6</sup>R. Humphreys, *Nucl. Phys.* **A182**, 580 (1972).
- <sup>7</sup>B. F. Rozsnyai, *Phys. Rev.* **124**, 860 (1961).
- <sup>8</sup>J. V. Noble, *Phys. Rev. C* **17**, 2151 (1978).
- <sup>9</sup>J. V. Noble, *Nucl. Phys.* **A329**, 354 (1979).
- <sup>10</sup>L. G. Arnold and B. C. Clark, *Phys. Lett.* **84B**, 46 (1979).
- <sup>11</sup>M. Jaminon, C. Mahaux, and P. Rochus, *Phys. Rev. Lett.* **43**, 1097 (1979).
- <sup>12</sup>M. Jaminon and C. Mahaux, in *Proceedings of the Conference on the Meson Theory of Nuclear Forces and Nuclear Matter, Bad Honnef, 1979*, edited by D. Schütte, K. Holinde, and K. Bleuler (Bibliographisches Institut AG, Zürich, 1980).
- <sup>13</sup>J. D. Walecka, *Ann. Phys. (N.Y.)* **83**, 491 (1974).
- <sup>14</sup>S. A. Chin, *Ann. Phys. (N.Y.)* **108**, 301 (1977).
- <sup>15</sup>M. Brittan, *Phys. Lett.* **79B**, 27 (1978).
- <sup>16</sup>L. D. Miller, *Phys. Rev. Lett.* **28**, 1281 (1972).
- <sup>17</sup>L. D. Miller and A. E. S. Green, *Phys. Rev. C* **5**, 241 (1972).
- <sup>18</sup>L. D. Miller, *Phys. Rev. C* **9**, 537 (1974).
- <sup>19</sup>L. D. Miller, MIT Report No. 487, 1975 (unpublished).
- <sup>20</sup>L. D. Miller, *Ann. Phys. (N.Y.)* **91**, 40 (1975).
- <sup>21</sup>R. Brockmann and W. Weise, *Phys. Rev. C* **16**, 1282 (1977).
- <sup>22</sup>R. Brockmann, *Phys. Rev. C* **18**, 1510 (1978).
- <sup>23</sup>J. Boguta and J. Rafelski, *Phys. Lett.* **71B**, 22 (1977).
- <sup>24</sup>J. Boguta and A. R. Bodmer, *Nucl. Phys.* **A292**, 413 (1977).
- <sup>25</sup>K. P. Lohs and J. Hüfner, *Nucl. Phys.* **A296**, 349 (1978).
- <sup>26</sup>F. R. Serr and J. D. Walecka, *Phys. Lett.* **79B**, 10 (1978).
- <sup>27</sup>B. D. Serot, *Phys. Lett.* **86B**, 146 (1979).
- <sup>28</sup>B. D. Serot and J. D. Walecka, *Phys. Lett.* **87B**, 172 (1979).
- <sup>29</sup>L. G. Arnold, B. C. Clark, R. L. Mercer, D. G. Ravenhall, and A. M. Saperstein, *Phys. Rev. C* **14**, 1878 (1976).
- <sup>30</sup>L. G. Arnold, B. C. Clark, and R. L. Mercer, *Phys. Rev. C* **19**, 917 (1979).
- <sup>31</sup>B. C. Clark, L. G. Arnold, and R. L. Mercer, *Bull. Am. Phys. Soc.* **23**, 571 (1978).
- <sup>32</sup>L. G. Arnold, B. C. Clark, and R. L. Mercer, *Bull. Am. Phys. Soc.* **24**, 575 (1979).
- <sup>33</sup>B. C. Clark (private communication).
- <sup>34</sup>A. Ingemarsson, *Phys. Scr.* **9**, 156 (1974).
- <sup>35</sup>W. T. H. van Oers, H. Haw, N. E. Davison, A. Ingemarsson, B. Fagerström, and G. Tibell, *Phys. Rev. C* **10**, 307 (1974).
- <sup>36</sup>A. Nadasen, P. Schwandt, P. P. Singh, A. D. Bacher, P. T. Debevec, W. W. Jacobs, M. D. Kaitchuck, and J. T. Meek, *Phys. Rev. C* (in press).
- <sup>37</sup>K. Erkelenz, K. Holinde, and R. Machleidt (unpublished).
- <sup>38</sup>K. Holinde, Report No. Nordita 79/16, 1978 (unpublished).
- <sup>39</sup>M. L. Goldberger and K. M. Watson, *Collision Theory* (Wiley, New York, 1964), p. 340.
- <sup>40</sup>N. F. Mott, *Proc. R. Soc. London* **A124**, 425 (1929).
- <sup>41</sup>N. F. Mott and H. S. W. Massey, *The Theory of Atomic Collisions*, 3rd ed. (Clarendon, Oxford, 1965), p. 228.
- <sup>42</sup>A. Messiah, *Quantum Mechanics* (North-Holland, Amsterdam, 1961), Sec. 20.33.
- <sup>43</sup>L. L. Foldy and S. A. Wouthuysen, *Phys. Rev.* **78**, 29 (1950).
- <sup>44</sup>J. D. Bjorken and S. D. Drell, *Relativistic Quantum Mechanics* (McGraw-Hill, New York, 1964), p. 46.
- <sup>45</sup>J. L. Friar, *Phys. Rev. C* **10**, 955 (1974).
- <sup>46</sup>J.-P. Jeukenne, A. Lejeune, and C. Mahaux, *Phys. Rep.* **25C**, 83 (1976).
- <sup>47</sup>W. T. H. van Oers, *Phys. Rev. C* **3**, 1550 (1971).
- <sup>48</sup>R. Brockmann (private communication).
- <sup>49</sup>J. L. Friar and J. W. Negele, *Advances in Nuclear Physics*, edited by M. Baranger and E. Vogt (Plenum, New York, 1975), Vol. 8, p. 219.
- <sup>50</sup>H. D. Wohlfahrt, E. B. Shera, M. V. Hoehn, Y. Yamazaki, G. Fricke, and R. M. Steffen, *Phys. Lett.* **73B**, 131 (1978).
- <sup>51</sup>J.-P. Jeukenne, A. Lejeune, and C. Mahaux, *Phys. Rev. C* **16**, 80 (1977).
- <sup>52</sup>W. T. H. van Oers and H. Haw, *Phys. Lett.* **45B**, 227 (1973).
- <sup>53</sup>I. Abdul-Jalil and D. F. Jackson, *J. Phys. G* **5**, 1699 (1979).
- <sup>54</sup>J. W. Negele, *Phys. Rev. C* **1**, 1260 (1970).
- <sup>55</sup>L. R. B. Elton, *Nucl. Phys.* **89**, 69 (1966).
- <sup>56</sup>J.-P. Jeukenne, A. Lejeune, and C. Mahaux, in *Proceedings of the International Conference on Nuclear Self-Consistent Fields, Trieste, 1975*, edited by G. Ripka and M. Porneuf (North-Holland, Amsterdam, 1975), p. 155.

- <sup>57</sup>R. C. Clark, L. G. Arnold, and R. L. Mercer, Bull. Am. Phys. Soc. 25, 520 (1980) and private communication.
- <sup>58</sup>P. Schwandt, Bull. Am. Phys. Soc. 24, 824 (1979) and private communication.
- <sup>59</sup>W. H. Furry, Phys. Rev. 50, 784 (1936).
- <sup>60</sup>L. G. Arnold, B. C. Clark, and R. L. Mercer, in contribution 4C6 to the 8th International Conference on High Energy Physics and Nuclear Structure, Vancouver, 1979 (unpublished).
- <sup>61</sup>A. E. S. Green, F. Riewe, M. L. Nack, and L. D. Miller, in *The Nuclear Many-Body Problem*, edited by F. Calogero and C. Ciofi degli Atti (Editrice Compositori, Bologna, 1973), p. 415.
- <sup>62</sup>F. D. Becchetti and G. W. Greenlees, Phys. Rev. 182, 1190 (1969).
- <sup>63</sup>F. A. Brieva and J. R. Rook, Nucl. Phys. A297, 206 (1978).
- <sup>64</sup>D. F. Jackson and I. Abdul-Jalil, J. Phys. G 6, 481 (1980).